

# Deep LMT/AzTEC millimeter observations of $\epsilon$ Eridani and its surroundings

M. Chavez-Dagostino<sup>1\*</sup> E. Bertone,<sup>1</sup> F. Cruz-Saenz de Miera,<sup>1</sup> J. P. Marshall,<sup>2,3</sup> G. W. Wilson,<sup>4</sup> D. Sánchez-Argüelles,<sup>1</sup> D. H. Hughes,<sup>1</sup> G. Kennedy,<sup>5</sup> O. Vega,<sup>1</sup> V. De la Luz,<sup>6</sup> W. R. F. Dent,<sup>7</sup> C. Eiroa,<sup>8,9</sup> A. Gómez-Ruiz,<sup>1</sup> J. S. Greaves,<sup>10</sup> S. Lizano,<sup>11</sup> R. López-Valdivia,<sup>1</sup> E. Mamajek,<sup>12</sup> A. Montaña,<sup>1</sup> M. Olmedo,<sup>1</sup> I. Rodríguez-Montoya,<sup>1</sup> F. P. Schloerb,<sup>4</sup> Min S. Yun,<sup>4</sup> J. A. Zavala,<sup>1</sup> M. Zeballos,<sup>1</sup>

<sup>1</sup>*Instituto Nacional de Astrofísica Óptica y Electrónica Luis Enrique Erro #1, CP 72840, Tonantzintla, Puebla, México*

<sup>2</sup>*School of Physics, University of New South Wales, Sydney NSW 2052, Australia*

<sup>3</sup>*Australian Centre for Astrobiology, University of New South Wales, Sydney, NSW 2052, Australia*

<sup>4</sup>*Department of Astronomy, University of Massachusetts, Amherst, MA 01003, USA*

<sup>5</sup>*Institute of Astronomy, University of Cambridge, Cambridge CB3 0HA, UK*

<sup>6</sup>*SciESMEX, Instituto de Geofísica, Unidad Michoacán, Universidad Nacional Autónoma de México, Antigua Carretera a Pátzcuaro 8701, Morelia, Michoacán, CP 58089, México*

<sup>7</sup>*ALMA SCO, Alonso de Córdova 3107, Vitacura, Casilla 763 0355, Santiago, Chile*

<sup>8</sup>*Departamento de Física Teórica, C-XI, Facultad de Ciencias, Universidad Autónoma de Madrid, Canto Blanco 28049, Madrid, Spain*

<sup>9</sup>*Astro-UAM, Unidad Asociada UAM - CSIC, Madrid, Spain*

<sup>10</sup>*School of Physics and Astronomy, Cardiff University, CF24 3AA, UK*

<sup>11</sup>*Instituto de Radio Astronomía y Astrofísica, Universidad Nacional Autónoma de México, Antigua Carretera a Pátzcuaro 8701, Morelia, Michoacán, CP 58089, México*

<sup>12</sup>*University of Rochester, Department of Physics and Astronomy, Rochester, NY, 14627-0171, USA*

Accepted . Received; in original form

## ABSTRACT

$\epsilon$  Eridani is a nearby, young Sun-like star that hosts a ring of cool debris analogous to the solar system's Edgeworth-Kuiper belt. Early observations at (sub-)mm wavelengths gave tentative evidence of the presence of inhomogeneities in the ring, which have been ascribed to the effect of a putative low eccentricity planet, orbiting close to the ring. The existence of these structures have been recently challenged by high resolution interferometric millimeter observations. Here we present the deepest single-dish image of  $\epsilon$  Eridani at millimeter wavelengths, obtained with the Large Millimeter Telescope Alfonso Serrano (LMT). The main goal of these LMT observations is to confirm (or refute) the presence of non-axisymmetric structure in the disk. The dusty ring is detected for the first time along its full projected elliptical shape. The radial extent of the ring is not spatially resolved and shows no evidence, to within the uncertainties, of dust density enhancements. Additional features of the 1.1 mm map are: (i) the presence of significant flux in the gap between the ring and the star, probably providing the first exo-solar evidence of Poynting-Robertson drag, (ii) an unambiguous detection of emission at the stellar position with a flux significantly above that expected from  $\epsilon$  Eridani's photosphere, and (iii) the identification of numerous unresolved sources which could correspond to background dusty star-forming galaxies.

**Key words:** circumstellar matter – (sub-)mm: stars.

## 1 INTRODUCTION

The circumstellar debris disks detected around mature, main sequence stars are a visible remnant of planet for-

mation processes (Backman & Paresce 1993). Composed of icy and rocky bodies ranging from micron-sized grains to kilometre-sized planetesimals, the presence of a disk is typically revealed through the detection of excess emission from the star at mid- and far-infrared wavelengths (Wyatt 2008; Matthews et al. 2014).

\* E-mail: mchavez@inaoep.mx (MC)

Recent surveys by the *Herschel* Space Observatory (Pilbratt et al. 2010) have identified cool disks, analogs to the Edgeworth-Kuiper belt of our solar system, in around  $20 \pm 2\%$  of Sun-like stars (Eiroa et al. 2013). However, their detection rate depended on both the temperature of the host star and on the observing strategy of the space craft. For instance, Thureau et al. (2014) found an incidence of 30% in A-type stars. The combination of exoplanet and debris disk surveys has provided evidence that planets are more common around stars that also host a debris disk (Bryden et al. 2013), and revealed tentative correlations linking the presence of dust and planets with the properties of the host star (Wyatt et al. 2012; Maldonado et al. 2012; Marshall et al. 2014a; Moro-Martín et al. 2015). The presence of a planet around a host star can be revealed through its dynamical interaction with the debris disk which creates non-axisymmetric structures (clumps, warps, cavities, etc.) in the disk. Such structures led to the discovery of a giant planetary companion in the prototypical debris disk host  $\beta$  Pictoris (Lagrange et al. 2010). Thermal emission from the micron sized dust grains dominates the observed flux of the disk at far-infrared wavelengths, and exhibits typical temperatures of 30 to 80 K (Morales et al. 2011) and radial size scales of 10s to 100s of astronomical units (AU) (Pawellek et al. 2014, see also Marshall et al. 2014a). Tracing the largest millimeter sized and coolest grains in the disk, which do not drift as far from their parent planetesimal belt under the action of radiation forces as the smaller micron sized grains (Krivov et al. 2008), is vital to accurately determine the location of the dust-producing belt of planetesimals around the star (Krivov 2010). Such measurements are only possible with (sub-)millimeter continuum imaging observations (e.g. Williams & Andrews 2006; Nilsson et al. 2010; Panić et al. 2013). Resolving the radial extent of the disk is fundamental in the modeling process as it directly constrains the orbital radius of the dust responsible for the observed emission, weakening inherent degeneracies between grain size and radial distance in those models reliant solely on the disk thermal emission derived from analyses of the spectral energy distribution (SED; Augereau et al. 1999; Lebreton et al. 2012; Ertel et al. 2014; Marshall et al. 2014b).

$\epsilon$  Eridani ("Ran", HR1084, HD22049, HIP16537) is a relatively young (age=0.8 Gyr, Di Folco et al. 2004; Mamajek & Hillenbrand 2008; 1.4 Gyr, Bonfanti et al. 2015), nearby ( $d = 3.22$  pc) Sun-like (spectral class K2V) star. Its age and distance place it as the closest isolated star of this kind where we can study the early stages in the evolution of a planetary system analogous to the solar system. The star is host to a bright, extended, almost face-on debris disk, which ranks amongst the finest examples of these objects so far discovered (Greaves et al. 1998; Holland et al. 1998). Recent models (Backman et al. 2009; Reidemeister et al. 2011) suggest that the disk is comprised of up to four distinct components: two warm inner belts, a cold outer belt and an extended halo of small grains. In these models the dust in the warm components actually originates in the the cold belt and is transported to the inner regions through the Poynting-Robertson drag and stellar winds. Radial velocity analyses suggest the existence of two giant exoplanets in addition to the warm inner debris disk (Hatzes et al. 2000; Moran et al. 2004). These planets are

inferred to be within a few AU of the star, however their existence still remains contentious due to the high level of activity of  $\epsilon$  Eridani, making interpretation of the spectroscopic measurements difficult (Zechmeister et al. 2013).

The cold outer belt of  $\epsilon$  Eridani has been extensively studied from far-infrared (FIR) to (sub-)mm wavelengths from the ground (Greaves et al. 1998; Schütz et al. 2004; Greaves et al. 2005; Backman et al. 2009; Lestrade & Thilliez 2015; MacGregor et al. 2015) and from space (Gillett 1986; Backman et al. 2009; Greaves et al. 2014). These observations showed that the debris disk has a ring-like morphology and provided the first estimates of the basic physical properties of the ring such as radial extent, width and inclination. Early sub-millimeter observations conducted with the SCUBA camera on the James Clerk Maxwell Telescope (JCMT, Greaves et al. 1998, 2005) also suggested that the ring has a clumpy structure that has been interpreted as evidence of dynamical interaction between an unseen planetary companion and the debris belt (Quillen & Thorndike 2002). Substructures in the ring were also identified in *Herschel*/PACS images at  $160 \mu\text{m}$  by Greaves et al. (2014) who, after considering limb brightening effects due to inclination, obtained a 10% flux residual when comparing the flux in the southern portion of the ring to that of the north. Additionally, recent deep (rms  $\sim 0.8$  mJy/beam) observations made with MAMBO on IRAM at 1.2 mm (Lestrade & Thilliez 2015) appear to corroborate the disk inhomogeneities found by SCUBA, though with one of the prominent clumps present in the SCUBA image being absent in the MAMBO map. The time span (18 years since the first sub-mm detection) between the different observational data sets and the large proper motion of  $\epsilon$  Eridani,  $1''/\text{yr}$ , have enabled studies of the outer belt's structure and dynamics, identifying which clumps in the belt could be associated with the disk and which might correspond to background sources, and to look for positional changes of the belt structures over time. The disk orbital motion has been estimated to be of the order of  $1^\circ/\text{yr}$  (Greaves et al. 2005) or three times as large (Poulton et al. 2006). There are, however, contrasting results. Observations at 1.2 mm with the bolometer array SIMBA on the SEST telescope (at a depth of 2.2 mJy/beam rms) did not confirm the presence of substructure in the ring (Schütz et al. 2004), in agreement with the very recent interferometric map at 1.3 mm collected with the Submillimeter Array (SMA) by MacGregor et al. (2015). They found that a smooth ring model could explain their patchy high resolution image. There are other examples in which the presence of dust density enhancements based on early observations at long wavelengths have been questioned by more recent high resolution imagery. Noteworthy is the case of the very prototypical object Vega for which SCUBA observations in the sub-mm revealed bright blobs (Holland et al. 1998), but whose detection was later disputed (e. g. Hughes et al. 2012).

Motivated by the debated presence of structure along the ring around  $\epsilon$  Eridani, its potential correlation with an inferred planet orbiting close to the inner edge of the ring, and the possibility of measuring the orbital motion of dust enhancements within the ring, we conducted deep continuum observations at 1.1 mm with the AzTEC instrument

on the Large Millimeter Telescope Alfonso Serrano<sup>1</sup> (LMT). In Section 2, we describe the LMT observations and reduction techniques. In Section 3, the global observational morphology of the ring is presented. Section 4 is devoted to the detailed modeling of the ring structure. In Section 5, we briefly discuss the spectra of the components of the system. Section 6 provides additional comments on the flux detected at the stellar position, and in Section 7 we briefly comment on the background sources towards the  $\epsilon$  Eridani's system. The concluding remarks are given in Section 8.

## 2 OBSERVATIONS AND DATA REDUCTION

Observations with the 1.1 mm continuum camera AzTEC (Wilson et al. 2008) were conducted in November and December 2014 as part of the Early Science Phase-3 of the LMT, while the 50-m diameter telescope was operating in its 32-m aperture configuration. The telescope is located on top of the extinct volcano Sierra Negra, in the state of Puebla, Mexico, at an altitude of 4600 m above sea level. A total of 18.5 hours on source were devoted to the target under weather conditions that ranged from excellent to good ( $\tau_{225\text{GHz}} = 0.03\text{--}0.11$ ). The field was observed with the AzTEC small-map observing mode which covers an area of about 7.5 arcmin<sup>2</sup>. The point spread function (PSF) of the instrument in this configuration has a FWHM beam size of 8.5'', however, filtering in the reduction process results in an effective resolution of 10.9''. We made observations of the quasar 0339-017 roughly every hour which bracketed our observations of the  $\epsilon$  Eridani field. The measured quasar pointing offsets (typically < 5'') were then interpolated in time to remove any offset and drift in pointing from the science observations.

The raw data were reduced using the standard AzTEC analysis pipeline and analysis approach (Scott et al. 2008; Wilson et al. 2008) but without applying the final Wiener filter that many AzTEC observations use for the optimal detection of point sources. Instead, the final unfiltered image was smoothed with a Gaussian filter with FWHM=6.8''. The data were flux calibrated based on observations of the protoplanetary nebula CRL618 and the noise in the final image is estimated from jackknifed time streams created as described in Scott et al. (2008).

Figure 1 displays the final AzTEC 1.1 mm map which has an rms of 0.20 mJy/beam, about ten times deeper than the SIMBA/SEST observations and four times deeper than those of MAMBO/IRAM. The scale of the map is 1''/pixel which results in 93 arcsec<sup>2</sup>/beam for the smoothed beam size of 10.9''. This superb depth reveals three main interesting features in the map: a well defined complete ring detected for the first time at millimeter wavelengths, a clearly detected central peak, and numerous unresolved background sources, some of which were present in previous maps, in particular those from SCUBA/JCMT and *Herschel*/PACS and SPIRE instruments (Poglitsch et al. 2010; Griffin et al. 2010). Below, we describe in more detail these characteristics.

## 3 MORPHOLOGY OF THE DUSTY RING

The ring is detected (at a significance ranging from 5.7 to 10.4 $\sigma$ ) at all position angles and displays an almost perfect elliptical shape oriented along a north-south direction. Fitting an elliptical ring to the image results in a major axis of 20.0'' (or 64 AU) and the minor axis of 16.9'' (54 AU), which implies an inclination for a circular ring of about 32°. This latter value is in agreement with the same 32° derived from *Herschel* data at 160  $\mu$ m (Greaves et al. 2014) and also, within their uncertainties, with the  $\sim 17(\pm 14.2)^\circ$  inclination estimated from the SMA map (MacGregor et al. 2015). The centroid of the ring matches the stellar position to within the expected pointing uncertainties of the LMT, therefore we conclude that no offset is detected between the ring and  $\epsilon$  Eridani.

The fact that we detect the full ring, clearly separated from a central peak, allows us to provide more observational constraints on the basic properties needed for the disk modeling, namely: the distance from the star (the ring radius  $R$ ), the ring width (upper limit), and the dust properties obtained through the integrated flux density. In unresolved disks, whose dust characteristics can only be inferred through analysis of the SED, some of the above derived properties are, as mentioned before, degenerate.

In addition to the ring radius  $R$  and the inclination mentioned above, the ring appears unresolved in the radial direction (width < 11'' or  $\sim 35$  AU) and has an integrated flux density, obtained through standard aperture photometry analysis, of  $27.7 \pm 3.3$  mJy, compatible with the values obtained at millimeter wavelengths with IRAM/MAMBO (Lestrade & Thilliez 2015) and the SMA (MacGregor et al. 2015).

Morphologically, the ring in the LMT map shows a prominent extended brightening in the SE and three apparent clumps in the NW. This SE flux enhancement is evident from the azimuthal flux peak distribution depicted with the red line of Figure 2. The maximum is at  $\sim 160$  degrees from the north counterclockwise reaching about 3.5 mJy/beam, which is  $\sim 50\%$  above the lowest flux levels of the ring in the 0–40 deg and 230–360 deg segments. This flux difference is certainly less notable than the factor of three reported in Greaves et al. (2005, their Fig. 3) and the factor of four in Lestrade & Thilliez (2015). This SE bright arc is neither seen in the MAMBO map nor in SMA data. Conversely, the apparent clump in the SW in the SCUBA and MAMBO maps is not seen in the LMT image. While there are discrepancies, it is important to note that the published SCUBA data provided the most complete ring maps in the imaging data collected prior to these LMT observations, and that the bright arc in the SE has been regarded as a real feature of the ring. Whilst a direct inspection of the positions of the flux maxima of this SE arc in the two SCUBA and the LMT images appear to indicate motion of substructures, the two sources east of the ring in the LMT map, in particular that labeled S3 in Figure 1, could conceivably explain the apparent flux enhancement in the SCUBA map of Greaves et al. (1998) as its position agrees with that of the ring at the time when the SCUBA observations were carried out. Similarly, the suggested background sources as the origin of the flux brightening in the SW in the first SCUBA map could now well partially contribute to the LMT SE brightening. In Fig-

<sup>1</sup> www.lmtgtm.org

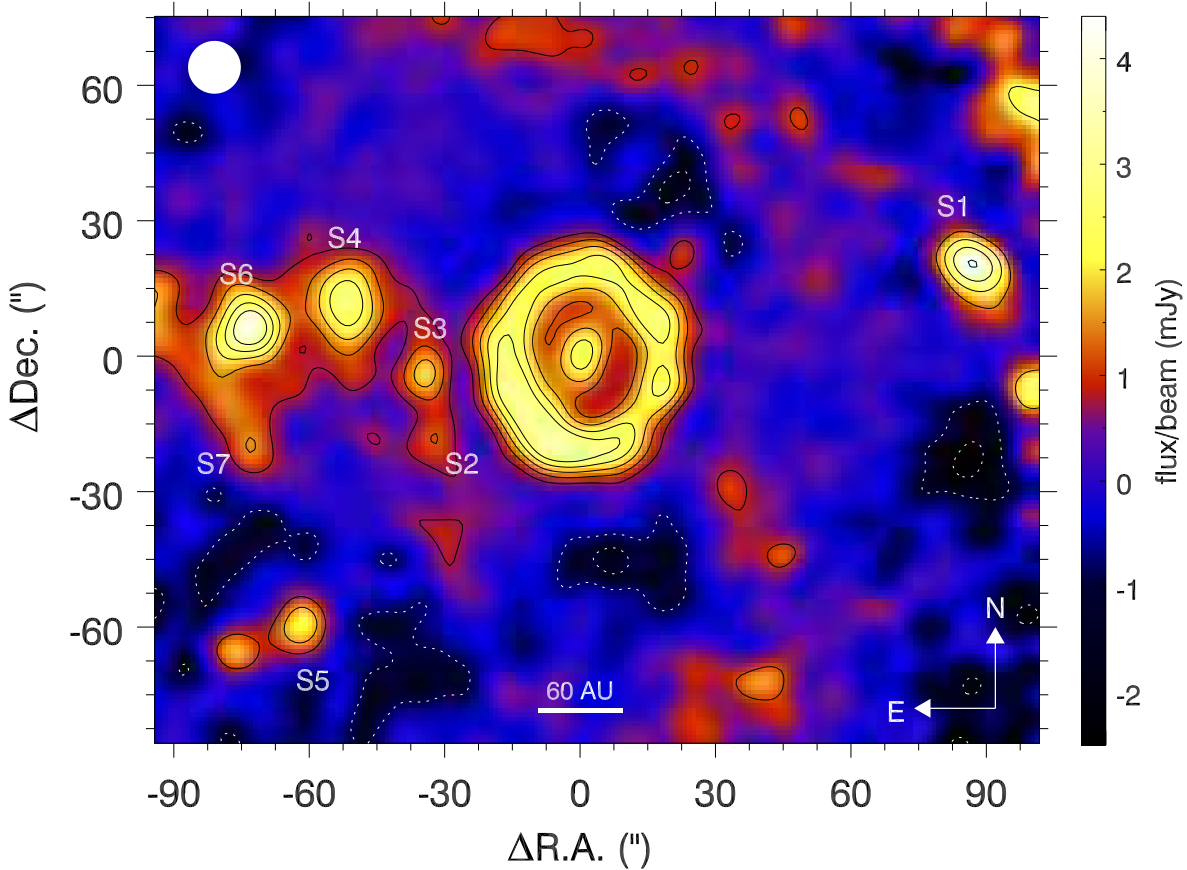


**Figure 1.** 1.1 mm LMT/AzTEC continuum map of  $\epsilon$  Eridani. The outer ring is fully detected at a significance of  $>5.7\sigma$ . The central peak is detected at  $7.5\sigma$  and likely corresponds to the sum of three contributing agents: the stellar photosphere, the stellar upper atmosphere and an (or perhaps two) inner warm disk(s). As many as seven (S1-S7) background objects are detected in this map, of which, four have  $S/N > 5$ . The source labeled S1 is the brightest with a 1.1 mm flux of  $4.6 \pm 0.6$  mJy. The smoothed beam size of  $10.9''$  FWHM is given by the white circle in the top-left. As a reference, we include the contour levels for  $S/N = -3.5, -2, 2, 3.5, 5.0, 6.5, 8.0$ .

ure 3 we show the positions of the dust ring with respect to the stationary background sources at different epochs correspondent to previous (sub-)mm observations.

To further verify the presence (or lack) of substructures along the ring, we modeled the  $\epsilon$  Eridani LMT image using optically thin debris disk models as presented below.

#### 4 $\epsilon$ ERIDANI MODELLING

We modeled the emission from  $\epsilon$  Eridani using a parameterized model of an optically thin debris disk. This model has been described in detail in Wyatt et al. (1999) and Kennedy et al. (2012). Basically, a 3D distribution of dust surface area is generated, which can be viewed from any direction to create synthetic images. The surface brightness of the images is calculated by adding up the emission in individual cells along the line of sight, where each cell emits like a blackbody at some temperature that is proportional to the distance to the central star. For the resolved disk components we used a temperature law of  $T_{\text{res}} = 416/\sqrt{R}$  K, where  $R$  is the disk radius in AU. Though we model the data at a single wavelength, this temperature was chosen to provide

a reasonable extrapolation of the model to the photometric data at other wavelengths. For debris disks this model can account for important effects such as brightening at disk ansae and brightness asymmetry for non-axisymmetric disks.

For a given model viewed at some orientation, a high resolution disk image is first generated. The central stellar emission of 0.7 mJy (i.e. the expected photospheric flux, see next section) is then added and the model is convolved with the LMT beam. A  $\chi^2$  goodness of fit metric is then computed within an  $80 \times 80''$  area shown in Figure 4, but only pixels (about 70%) where the emission from either the model or the image is significant are used (for details see Wyatt et al. 2012). The variable background level means that simple least squares minimization does not necessarily yield satisfactory results, so in most cases some by-hand intervention was needed to obtain a smooth and continuous background. That is, even though models with  $\chi^2$  values lower than those presented are possible, they remove what could be astrophysical background behind the disk, in particular at the SE side, and produce negative residuals in the NW. While the  $\chi^2$  is always several times higher than the number of degrees of freedom (because our model of the sky



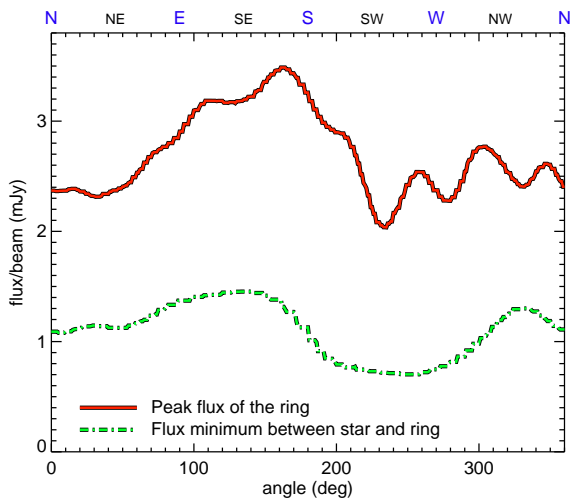


**Figure 2.** Azimuthal flux distribution showing the variations of the flux maxima along the ring (continuous line). On average, the ring flux has a level of 2.4 mJy/beam, and the brightest arc of the ring is in the SE as can be seen in the map of Figure 1. The flux peak in this bright arc is  $\sim 3.5$  mJy at about 160 degrees, measured counter-clockwise from north. The green dot-dashed line indicates the flux distribution in the gap which is also fully detected. The SE-NW ansae seen in Fig. 1 corresponds to the bumps in the gap distribution. The origin of this brightening is not known, but can plausibly be a reduction artifact.

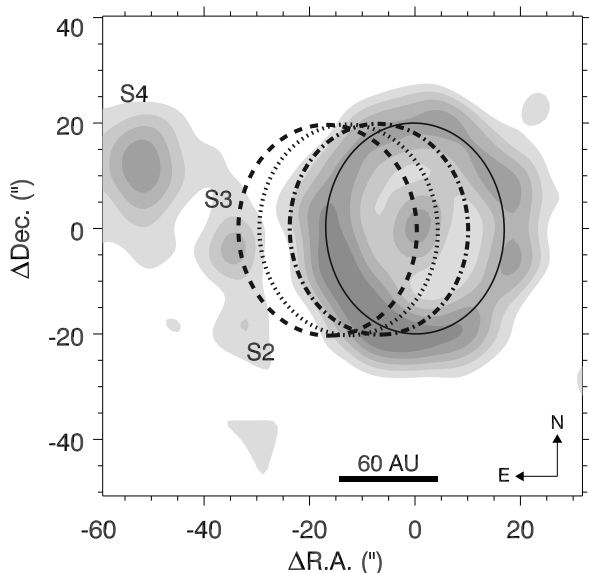


**Figure 3.** Zoomed version of the 1.1 mm LMT/AzTEC continuum map of  $\epsilon$  Eridani. The map is presented in gray scales that correspond to the contour levels of Figure 1. The ellipses denote the ring positions at different epochs with respect to background point sources due to the proper motion of the system. The ellipses with thin solid, dot-dashed, dotted, and dashed lines show the location of the  $\epsilon$  Eridani system at the epochs of the observations with AzTEC (2014.9), MAMBO (2007.9), and SCUBA (2002.0, 1997.9), respectively. Note that the source S3 almost coincides with the ring position at the first SCUBA observations of Greaves et al. (1998).

near  $\epsilon$  Eri is incomplete), visually better fitting models do have lower  $\chi^2$  values. As is commonly the case with models of low spatial-resolution data, we do not explore all possible parameter space so do not claim that our models are unique, but that they are reasonable interpretations of the LMT data.

The outer ring at  $\sim 70$  AU is clear in the LMT image, so the main goals of the modeling were i) to determine whether the ring width was well constrained, ii) determine whether additional emission above that expected from the star is present interior to the outer ring, and iii) look for any evidence of azimuthal structure.

Additional issues for this modeling were the overall flux calibration and any flux (DC) offset, and nearby background sources. We allowed for a small DC offset in modeling the images, though it did not influence the results. Near the disk three background sources were added, one corresponding to the blob in the NW, and two to the E and SE sources labelled S3 and S2 in Figure 1, respectively. As we note below, there is the possibility of additional emission that exists behind the SE portion of the disk, which could plausibly be an extension of the diffuse emission to the E of the system.

#### 4.1 Ring width

To address point i) above, we constructed models with a range of ring widths with constant surface density centered at a distance of about 70 AU from the star. These models consider an inclination of  $30^\circ$  which, unlike previous observational results at millimeter wavelengths (e.g. MacGregor et al. 2015), is strongly constrained. The position angle is  $7^\circ$  from north to west (i.e. slightly west of north), so the geometry is consistent with previous results (Greaves et al. 2014; MacGregor et al. 2015). Models with arbitrarily narrow ring widths reproduced the data reasonably well, with  $\chi^2_{\text{red}}$  values of around 4.7 (where  $\chi^2_{\text{red}}$  is the reduced  $\chi^2$ ), and these models also have a good fit to the dust emission interior to the main ring. We also constructed models with wide rings, finding that a width of up to 30 AU was acceptable, but for larger sizes the ring surface brightness becomes too low, i.e. for a 30 AU width  $\chi^2_{\text{red}} = 5$ . Some example models are shown in Figure 4. The lower two rows of panels show the results for narrow (10 AU) and wide (30 AU) outer belts, both of which produce reasonable results. Thus, we conclude that the LMT image does not place a lower limit on the ring width and that it could be as wide as 30 AU, conclusions that compare well with those of Lestrade & Thilliez (2015) and MacGregor et al. (2015).

#### 4.2 Non-stellar emission interior to the ring

To address the second issue, we constructed models with an additional interior component. The inclusion of this extra component is motivated by two facts: 1) we expect a contribution of an excess above the photosphere from the star originating from the warm belt(s) and 2) the significant flux in the gap between the star and the ring we found in the LMT map (green dot-dashed line in Figure 2).

The width and brightness of this component was varied to ascertain whether its existence was required by the data, and if so, the extent of this component. The above models

that include only the outer belt leave significant residuals in the interior regions ( $\chi^2_{\text{red}} = 8.2$ ), so we conclude that mm-wave emission exists in excess of the stellar photospheric emission interior to the outer belt (e.g. top row of panels in Figure 4). A 2.7 mJy (i.e. 2 mJy above the photosphere) point source at the stellar position produces marginally satisfactory results ( $\chi^2_{\text{red}} = 5.3$ ), but emission remains between the star and the outer belt (second row of panels). The same conclusion can be reached by considering the radial flux distribution shown in Figure 5, where the outer belt appears unresolved but the interior flux cannot be explained by simply adding a point source at the star position. This flux is somewhat overestimated, as can be seen by the negative residuals at the star position. We therefore favour models with extended emission between the star and the outer belt. Models with interior emission included can reproduce the data fairly easily; both continuous emission from a flat surface density disk extending from 14 to 63 AU, and a narrow belt at 30 AU produced satisfactory results ( $\chi^2_{\text{red}} \approx 4.7$  (see the third and fourth rows in Figure 4). Thus, while we are confident that the interior emission exists, we cannot constrain from where this emission originates. In most models a small amount of emission was required at the stellar position, but the level is degenerate with the structure of the emission between the star and the outer belt.

### 4.3 Azimuthal structure

In all cases where a reasonable fit to the data was obtained there was no evidence for significant non-axisymmetric emission in the residuals. In most cases emission remained in the SE part of the ring, but, given the extended structure seen to the E of the system, attributing this residual emission to the  $\epsilon$  Eridani system is not well justified.

Complementarily, we carried out a similar analysis as that of MacGregor et al. (2015), namely, we calculated the residual emission by subtracting a best fit model of the ring to the integral of the observational flux calculated in sectors with a central angle of  $10^\circ$  extending from  $10''$  to  $28''$  from the center. Note that the outer radius of the annulus is slightly smaller than in MacGregor et al. (2015) because we wanted to avoid contamination from the faint NW source close to the ring. The azimuthal distribution of the residual flux is displayed in Figure 6. Note that the only potential feature detected in the NE quadrant of the SMA map is not present in our map. To within the uncertainties, the distribution shown in this figure indicates that the ring has a smooth structure, with perhaps the presence of two regions of low flux at azimuthal angles of  $\sim 220$  and  $\sim 320$  degrees.

The various components in the best fit models have a 1.1 mm flux of  $\sim 25$  mJy for the outer ring, in good agreement with the photometric result shown above, and a total of 5.5 mJy for the interior regions. A flux of 0.7 mJy is attributed to the stellar photosphere. For the model where the interior disk component is a narrow ring the flux is 3.4 mJy, and when it is extended the flux is 4.5 mJy.

## 5 THE SPECTRUM OF THE $\epsilon$ ERIDANI SYSTEM

The infrared to millimeter spectrum of the  $\epsilon$  Eridani system is depicted in Figure 7. Three separate components are shown in this figure. The solid brown line represents the photosphere that was generated from an interpolation within the library of synthetic spectra of Castelli & Kurucz (2003). These synthetic fluxes are calculated up to  $160 \mu\text{m}$ , so an extrapolation of the Rayleigh-Jeans tail was necessary to account for the flux at longer wavelengths. We have assumed the stellar parameters derived by Paletou et al. (2015):  $(T_{\text{eff}}/\log g/[\text{Fe}/\text{H}] = (5034/4.51/+0.16))$ . The dashed curve indicates the location of the modified blackbody curve for a temperature of 48 K,  $\lambda_0 = 150 \mu\text{m}$ , and an emissivity index  $\beta = 0.4$  (Greaves et al. 2014). Ancillary data (see labels in the figure) are also plotted for illustrative purposes and no formal fit of the points was attempted. The data, in spite of some dispersion, are well represented by the above modified blackbody parameters. The dispersion can be partially attributable to the differing components that are included in the integrated flux densities calculated from distinct data sets. The dotted curve displays the best fit provided by the *Herschel*, SMA and LMT data for the inner component. The latter data point (1.3 mJy) includes only the unresolved central emission after subtracting the photospheric (and chromospheric, see next section) contribution considering  $\lambda_0 = 150 \mu\text{m}$ . The resulting best fit parameters of the warm component are  $T = 113$  K and  $\beta = 1.0$ . The blue line shows the extension of the modified blackbody for the inner component using the parameters of Greaves et al. (2014). The solid thick black curve corresponds to the summed contributions of the photosphere, the inner flux peak, and outer belt.

With the available data, dust masses ( $M_{\text{dust}}$ ) can be calculated for the different components. As in Greaves et al. (1998), we consider two cases for the absorption coefficient;  $k_{850\mu\text{m}} = 1.7$  and  $0.4 \text{ cm}^2\text{gr}^{-1}$  which at 1.1mm correspond to  $k_{1.1\text{mm}} = (850/1100)^\beta \times k_{850\mu\text{m}} \text{ cm}^2\text{g}^{-1}$ . At a distance of 3.22 pc,  $T = 48$  K, and  $\beta = 0.4$  ( $k_{1.1\text{mm}} = 1.53$  and  $0.36 \text{ cm}^2\text{g}^{-1}$ ),  $M_{\text{dust}}$  for the cold outer belt is 0.0035 and 0.015  $M_\oplus$ , which are slightly smaller, but compatible with those reported by Greaves et al. (1998).

For the inner component we conducted two calculations: a) we first considered the best fit parameters obtained above for the unresolved warm component and the transformed absorption coefficients  $k_{1.1\text{mm}} = 1.31$  and  $0.31 \text{ cm}^2\text{g}^{-1}$  for  $\beta = 1.0$ . The resulting  $M_{\text{dust}}$  are  $7.6 \times 10^{-5}$  and  $0.0003 M_\oplus$  for the two coefficient values, respectively; b) we assumed an inner component that includes both the unresolved component and a narrow warm disk with a total flux of 3.4 mJy, in agreement with an emissivity index of  $\beta = 0.4$ . In this case the dust mass is  $M_{\text{dust}} = 0.00017$  and  $0.0007 M_\oplus$ , for the high and low values of  $k_{1.1\text{mm}}$ , respectively. According to these results there is a similar amount of warm dust ( $0.0001 M_\oplus$ ) very close to the star and in between the central unresolved emission and the external cold belt which could be, as mentioned before, evidence of material being transported to the inner regions from the outer relatively massive debris ring.

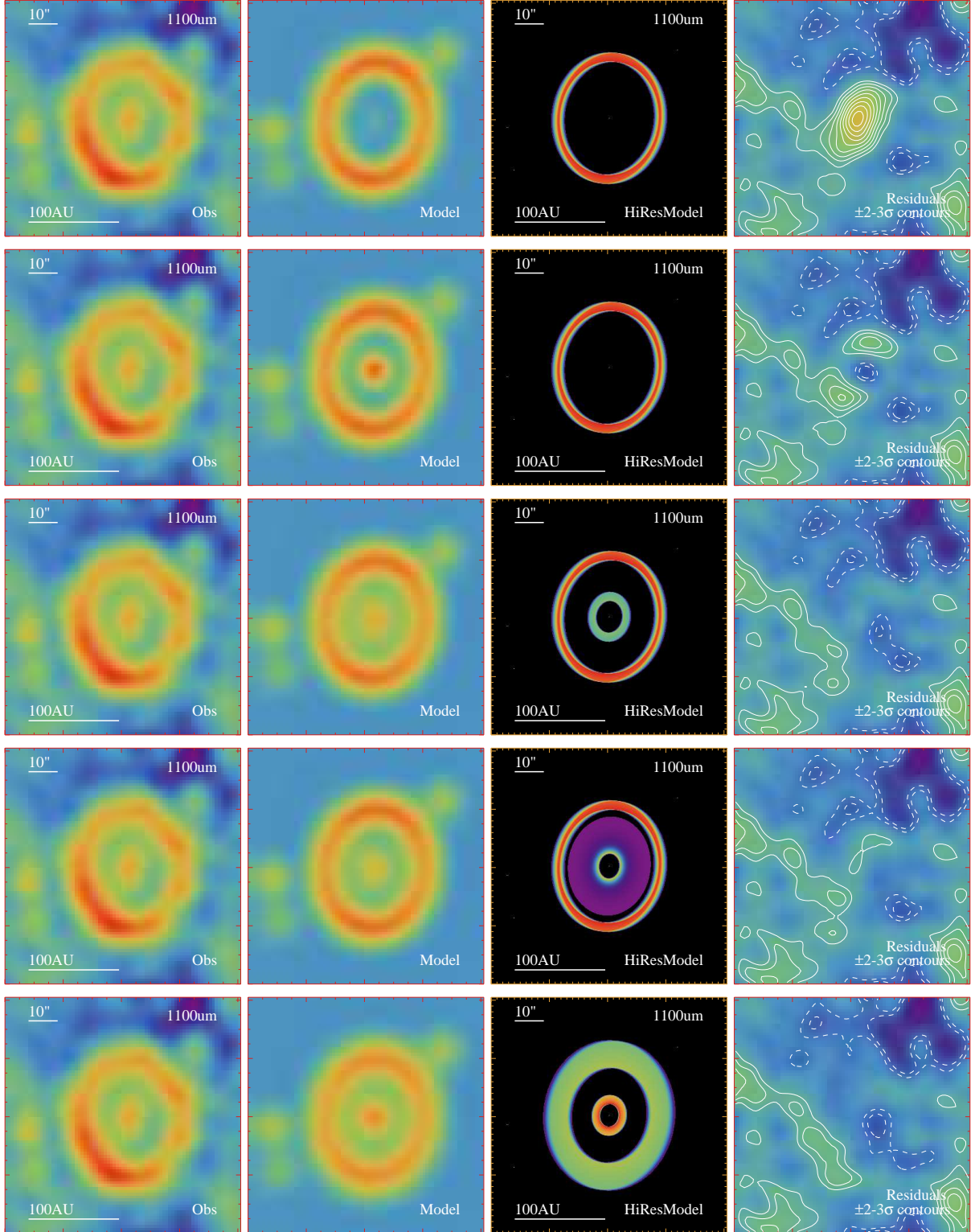


**Figure 4.** Models of the LMT 1.1 mm image of  $\epsilon$  Eridani. Each row is a different model, with the panels showing, from left to right, the data, the model at the resolution of the 32-m LMT, the high resolution model, and the residuals. The residuals include contours in units of S/N from  $\pm 2\sigma$ . The panels of the first and second rows show an outer ring centered at 68 AU and 10 AU wide, with the stellar photosphere (0.7 mJy) as the only contributor in the inner region (first row), and an artificial point source of 2.7 mJy added at the stellar position (second row). The third row considers an outer ring as in the above panels and includes an inner ring 10 AU wide at 23 AU. In the fourth row the inner component is wider, extending from 14 to 63 AU, but follows a surface density power law with index  $-3.5$  in order to keep it concentrated. In the bottom row panels we considered a wider (30 AU) outer ring centered at 69 AU, with a narrow (10 AU) inner component at 18 AU.

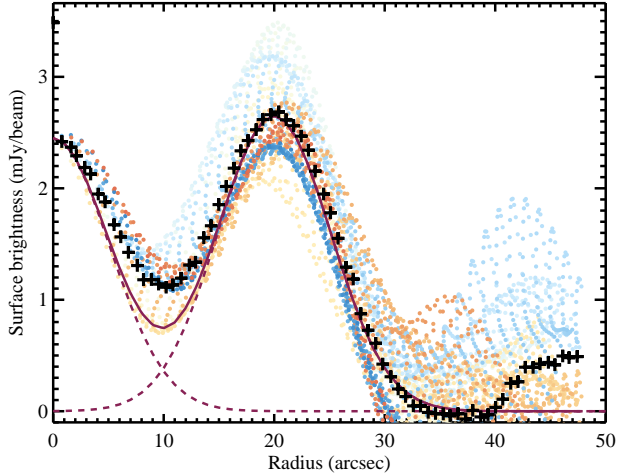


**Figure 5.** Radial flux distribution of the  $\epsilon$  Eridani system. The dotted lines are the Gaussian profiles fitted to the central peak and the ring. They both match the PSF of  $11''$ , hence not resolved. The continuous line is the sum of these profiles. Colored dots represent the full set of flux points in each azimuthal direction, and the average observed fluxes are depicted with the “+” symbols. Note that significant diffuse flux is present in the gap at  $10''$  radius.

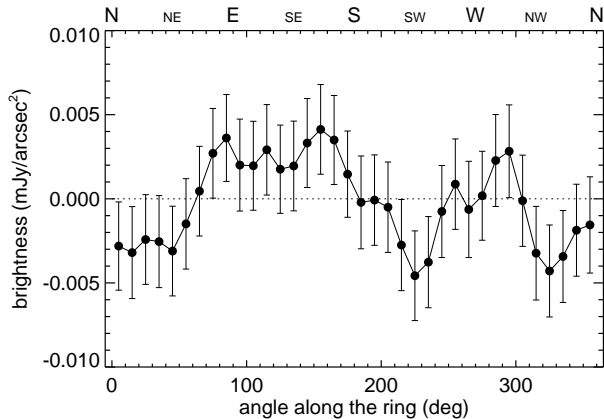


**Figure 6.** Flux residual obtained by subtracting a well fitting model flux to that of the observed map. The residual indicates that, to within the uncertainties, the ring has a smooth morphology. A reduced  $\chi^2$  of the data points results in 0.92, supporting lack of substructures.

## 6 ADDITIONAL COMMENTS ON THE CENTRAL PEAK

The unresolved emission from the central peak is detected at  $7.5\sigma$ . The integrated flux in the center is  $2.3 \pm 0.3$  mJy and arises from several potential contributors, namely, the stellar atmosphere (photosphere and chromosphere) and the Rayleigh-Jeans tail of the warm dust component(s) identified at 70 and  $160 \mu\text{m}$  with *Herschel*/PACS (Greaves et al. 2014). As mentioned above, the expected photospheric contribution to the total flux at 1.1 mm is 0.7 mJy, implying a potential warm dust contribution of  $\sim 1.6$  mJy. The blue line in Figure 7 predicts an excess of  $\sim 3.5$  mJy at 1.1 mm, which is nearly twice as much as that measured in our LMT map. In fact, the addition of the two extra data points pro-

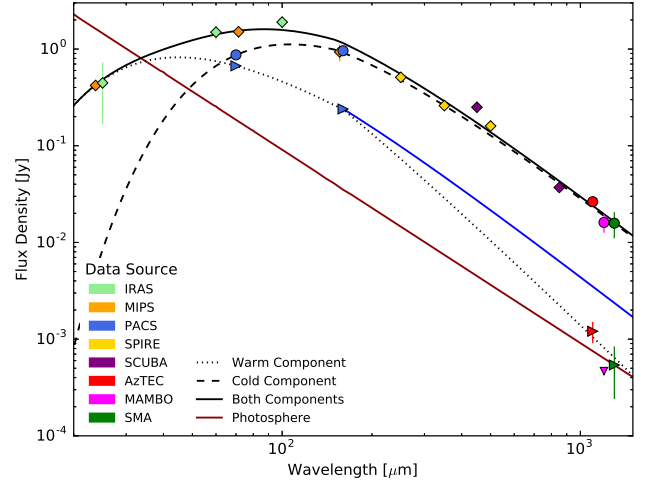


**Figure 7.** Spectrum of  $\epsilon$  Eridani. Different lines styles represent the different components of the system: the photosphere (solid red), the outer belt (dashed), the inner component (dotted), and the summed contributions (thick solid). The instrumental origin of the ancillary data is indicated in the figure inset and the symbols stand for data that contain fluxes for the inner component (triangles), the outer belt (circles), and those of the whole system (diamonds). These data have been partially compiled by Greaves et al. (2014) from Backman et al. (2009) and Greaves et al. (2005). The outer belt spectrum has been constructed with the parameters  $T=48$  K,  $\lambda_0=150 \mu\text{m}$ , and  $\beta = 0.4$ , as in Greaves et al. (2014). The inner component, instead, represents the best fit of the four available points, two from *Herschel* PACS at 70 and  $160 \mu\text{m}$ , the SMA data point at 1.3 mm, and the LMT/AzTEC flux at 1.1 mm. The best fitting parameters assuming  $\lambda_0=150 \mu\text{m}$  are  $T=113$  K and  $\beta = 1.0$ . The solid blue line shows the long wavelength extension of the gray body emission for the inner component considering an emissivity index of  $\beta = 0.4$ . The two data points at long wavelengths (and the upper limit of MAMBO at 1.2 mm) provide meaningful constraints on the dust properties of the warm belt.

vided by the LMT and the SMA results in a much steeper  $\beta$  index and suggests that  $\lambda_0$  should remain close to the *Herschel*/PACS band at  $160 \mu\text{m}$ . In addition, it has been found that active stars present a non-monotonic temperature variation towards the upper atmospheric layers, in a similar way the Sun displays a temperature increase towards low optical depths after reaching a minimum temperature in the atmosphere at about  $\log \tau = -4$ . This temperature gradient reversal is commonly evidenced by an excess in the ultraviolet regime but also as an atmospheric (sub-)mm-wave excess. In a recent study, Liseau et al. (2015) found that  $\alpha$  Cen B (K1 V) displays an excess at bands 9, 7 and 3 ( $440 \mu\text{m}$ ,  $870 \mu\text{m}$  and 3 mm, respectively) of the Atacama Large Millimeter/submillimeter Array (ALMA). Considering that  $\alpha$  Cen B and  $\epsilon$  Eridani have similar spectral types and assuming that both stars have a similar degree of activity, as suggested by their far and mid-ultraviolet (1200–2500 Å) continuum flux surplus, it is not unreasonable to expect a similar excess in  $\epsilon$  Eridani. The comparison of observed and predicted fluxes of  $\alpha$  Cen B indicates that in ALMA bands 7 and 3 the observed stellar fluxes are, respectively, 40 and 220% higher than predicted for the photosphere. Based on observations conducted with the Australia Telescope Com-



compact Array (ATCA) at 7 mm, MacGregor et al. (2015) reported a flux excess of about a factor of three, which agrees with the trend of an increasing excess at longer wavelengths. These authors argue that no plausible inner disk scenario is able to explain the observed excess and ascribe it to a thermal origin in the upper atmosphere of  $\epsilon$  Eridani. An interpolation of the bracketing ALMA points to the 1.1 mm band results in an excess of  $\sim 50\%$ , which would imply a total stellar flux of  $\sim 1$  mJy for  $\epsilon$  Eridani. This atmospheric value actually leaves 1.3 mJy at 1.1 mm originating from the unresolved warm belt(s) and, therefore, its contribution would be about half of the measured central emission. Complementing the LMT and SMA data with measurements of the central source at other (sub-)mm bands will be very valuable to better assess the appropriate contributions of the sources of millimeter emission. These contributions will allow us to better constrain the dust properties of the warm belt and to understand the outer atmospheric structure of  $\epsilon$  Eridani.

## 7 BACKGROUND SOURCES

As mentioned before, another important feature of our map is that, thanks to the depth and enhanced resolution achieved, we found numerous sources whose nature has been suggested, but never been previously investigated. In addition to the cold ring and the central peak, seven point sources were detected with a significance  $\geq 3.5\sigma$  and fluxes that range from 1.2 to 4.6 mJy (see Table 1). These sources do not have near- or mid-IR counterparts on either 2MASS or *WISE* images, but some are also present in previous *Spitzer* (Rieke et al. 2004, MIPS-70  $\mu\text{m}$ ), *Herschel* (PACS and SPIRE at 70, 160, 250, 350 and 500  $\mu\text{m}$ ), and, particularly, in SCUBA and SCUBA-2 images at 450 and 850  $\mu\text{m}$ . For several of the sources (S2, S3, and S7) our map provides the first detection. It has been suggested by Greaves et al. (1998, 2005) that these sources are probably members of the population of distant and heavily obscured sub-millimeter galaxies (SMG; Smail et al. 1997; Hughes et al. 1998). Considering the area of the map, we expect  $\sim 10$  SMGs to be present in our map for a detection threshold of  $S_{1.1\text{mm}} = 0.7$  mJy (Scott et al. 2012, Shimizu, Yoshida & Okamoto 2012), which is consistent with the number of point sources detected in the AzTEC map. It also agrees with the number counts derived in the very recent study of Fujimoto et al. (2016) scaled to the 1.1 mm wavelength for a spectral index of 3. The analysis of these background sources is beyond the scope of this paper. We, nevertheless, would like to remark that photometric and molecular line studies are required to reveal the (distant or nearby) nature of the sources surrounding the high Galactic latitude ( $|b| = 48^\circ$ ) target  $\epsilon$  Eridani.

## 8 SUMMARY AND CONCLUSIONS

We present the deepest (0.2 mJy rms) single dish observations at millimeter wavelengths of the prototypical debris disk target  $\epsilon$  Eridani conducted with the AzTEC camera on the LMT. Our 7.5 arcmin<sup>2</sup> image reveals the stellar emis-

**Table 1.** Positions and flux densities of background sources.

Source	offset RA [ $''$ ]	offset DEC [ $''$ ]	Flux [mJy/beam]
Central peak	...	...	$2.3 \pm 0.3$
S1	85.9	20.0	$4.6 \pm 0.6$
S2	-32.5	-18.7	$1.2 \pm 0.3$
S3	-34.5	-4.4	$1.9 \pm 0.3$
S4	-52.0	11.4	$3.0 \pm 0.3$
S5	-62.0	-59.7	$2.3 \pm 0.4$
S6	-73.1	5.6	$4.2 \pm 0.4$
S7	-73.1	-20.0	$1.5 \pm 0.3$

Offsets are given with respect to the stellar position. At the time of the observations (2014.9)  $\epsilon$  Eridani coordinates were  $\alpha = 03:40:13.1$  and  $\delta = -09:24:38.6$  which include a correction for proper motion of  $\mu_\alpha = -975.2$  mas/yr and  $\mu_\delta = 19.5$  mas/yr.

sion, the cool disk, and nearby (line-of-sight) environment with the following features:

- The ring is detected for the first time at all position angles. The ring has a measured radius of  $20''$  or 64 AU, and an upper limit of the width of 30 AU derived from model fitting, which implies a relative ring width ( $\Delta R/R$ ) of  $\leq 0.5$ . These values are in agreement with previous observational and modeled properties. The ring shows some inhomogeneities that could be explained by the presence of background objects that coincide with the ring position. Bright structures in the ring previously observed at comparable sub-mm wavelengths with SCUBA, can also be ascribed to background objects, currently separated from the ring due to the star's high proper motion. Modeling of the ring indicates that its morphology is essentially smooth, and that a potential residual brightening in the SE might be an extension of the diffuse emission east from the system.
- The central peak, which includes a stellar contribution and one or perhaps two warm dust belts is also clearly detected. These LMT observations, along with the recent SMA data and archival *Herschel* fluxes at 70 and 160  $\mu\text{m}$ , where the resolution is also good enough to separate the outer ring and the central peak, indicate that the interior warm dust contributes approximately 60% of this emission. The theoretical analysis of both the central peak and the outer dust ring shows evidence of significant emission in the gap. This may constitute the first evidence of the Pointing-Robertson drag outside the solar system.
- Numerous point sources are detected around the  $\epsilon$  Eridani system. The sources most likely correspond to a population of massive distant star-forming galaxies as has been suggested in previous works. Further analyses are needed to verify the nature and the properties of their cool dust component.

Our 1.1 mm observations demonstrate the current capabilities of the operational LMT in the study of nearby circumstellar debris disks. We have traced the full extent of the nearest debris disk/Edgeworth-Kuiper belt analog to the solar system for the first time. At the same time we have identified a number of line-of-sight background sources, which could be members of the sub-mm bright, high redshift population of star-forming galaxies. Disentangling these ex-

tragalactic sources from excesses around disk-host stars is critical for the proper interpretation of planetary systems analogous to our own. The LMT is expected to operate at its full aperture capacity of 50 meters in 2017. The resolution to be achieved in this final 50-m diameter configuration of the LMT is 5'', and when combined with the increased sensitivity, stronger constraints on the ring properties will be observationally established.

## ACKNOWLEDGMENTS

This work would have not been possible without the long-term financial support from the Mexican Science and Technology Funding Agency, CONACyT (Consejo Nacional de Ciencia y Tecnología) during the construction and operational phase of the Large Millimeter Telescope Alfonso Serrano, as well as support from the US National Science Foundation via the University Radio Observatory program, the Instituto Nacional de Astrofísica, Óptica y Electrónica (INAOE) and the University of Massachusetts, Amherst (UMass). MC, EB, FCSM, MO and RLV work was supported by CONACyT research grants SEP-2009-134985 and SEP-2011-169554. GMK is supported by the Royal Society as a Royal Society University Research Fellow. CE is partly supported by Spanish grant AYA2014-55840-P. JPM is supported by a UNSW Vice Chancellor's Postdoctoral Fellowship. SL acknowledges support from CONACyT through grant 238631. We are grateful to all of the LMT personnel and observers from Mexico and UMass who made possible this project.

## REFERENCES

- Augereau J. C., Lagrange A. M., Mouillet D., Papaloizou J. C. B., Grorod P. A., 1999, *A&A*, **348**, 557
- Backman D. E., Paresce F., 1993, in Levy E. H., Lunine J. I., eds, *Protostars and Planets III*. pp 1253–1304
- Backman D., et al., 2009, *ApJ*, **690**, 1522
- Bonfanti A., Ortolani S., Piotto G., Nascimbeni V., 2015, *A&A*, **575**, A18
- Bryden G., et al., 2013, in *American Astronomical Society Meeting Abstracts #221*. p. 144.24
- Castelli F., Kurucz R. L., 2003, in Piskunov N., Weiss W. W., Gray D. F., eds, *IAU Symposium Vol. 210, Modelling of Stellar Atmospheres*. p. A20
- Di Folco E., Thévenin F., Kervella P., Domiciano de Souza A., Coudé du Foresto V., Ségransan D., Morel P., 2004, *A&A*, **426**, 601
- Eiroa C., et al., 2013, *A&A*, **555**, A11
- Ertel S., et al., 2014, *A&A*, **561**, A114
- Fujimoto S., Ouchi M., Ono Y., Shibuya T., Ishigaki M., Nagai H., Momose R., 2016, *ApJS*, **222**, 1
- Gillett F. C., 1986, in Israel F. P., ed., *Astrophysics and Space Science Library Vol. 124, Light on Dark Matter*. pp 61–69, doi:10.1007/978-94-009-4672-9\_10
- Greaves J. S., et al., 1998, *ApJ*, **506**, L133
- Greaves J. S., et al., 2005, *ApJ*, **619**, L187
- Greaves J. S., et al., 2014, *ApJ*, **791**, L11
- Griffin M. J., et al., 2010, *A&A*, **518**, L3
- Hatzes A. P., et al., 2000, *ApJ*, **544**, L145
- Holland W. S., et al., 1998, *Nature*, **392**, 788
- Hughes D. H., et al., 1998, *Nature*, **394**, 241
- Hughes A. M., et al., 2012, *ApJ*, **750**, 82
- Kennedy G. M., et al., 2012, *MNRAS*, **421**, 2264
- Krivov A. V., 2010, *Research in Astronomy and Astrophysics*, **10**, 383
- Krivov A. V., Müller S., Löhne T., Mutschke H., 2008, *ApJ*, **687**, 608
- Lagrange A.-M., et al., 2010, *Science*, **329**, 57
- Lebreton J., et al., 2012, *A&A*, **539**, A17
- Lestrade J.-F., Thilliez E., 2015, *A&A*, **576**, A72
- Liseau R., et al., 2015, *A&A*, **573**, L4
- MacGregor M. A., Wilner D. J., Andrews S. M., Lestrade J.-F., Maddison S., 2015, *ApJ*, **809**, 47
- Maldonado J., Eiroa C., Villaver E., Montesinos B., Mora A., 2012, *A&A*, **541**, A40
- Mamajek E. E., Hillenbrand L. A., 2008, *ApJ*, **687**, 1264
- Marshall J. P., et al., 2014a, *A&A*, **565**, A15
- Marshall J. P., et al., 2014b, *A&A*, **570**, A114
- Matthews B. C., A. V. Krivov M. C. W., Bryden G., Eiroa C., 2014, in Beuther H., Klessen R. S., Dullemond C. P., Henning T., eds, *Space Science Series, Protostars and Planets VI*. The University of Arizona Press, pp 521–544
- Morales F. Y., Rieke G. H., Werner M. W., Bryden G., Stapelfeldt K. R., Su K. Y. L., 2011, *ApJ*, **730**, L29
- Moran S. M., Kuchner M. J., Holman M. J., 2004, *ApJ*, **612**, 1163
- Moro-Martín A., et al., 2015, *ApJ*, **801**, 143
- Nilsson R., et al., 2010, *A&A*, **518**, A40
- Paletou F., Böhm T., Watson V., Trouillet J.-F., 2015, *A&A*, **573**, A67
- Panić O., et al., 2013, *MNRAS*, **435**, 1037
- Pawellek N., Krivov A. V., Marshall J. P., Montesinos B., Abraham P., Moór A., Bryden G., Eiroa C., 2014, *ApJ*, **792**, 65
- Pilbratt G. L., et al., 2010, *A&A*, **518**, L1
- Poglitsch A., et al., 2010, *A&A*, **518**, L2
- Poulton C. J., Greaves J. S., Collier Cameron A., 2006, *MNRAS*, **372**, 53
- Quillen A. C., Thorndike S., 2002, *ApJ*, **578**, L149
- Reidemeister M., Krivov A. V., Stark C. C., Augereau J.-C., Löhne T., Müller S., 2011, *A&A*, **527**, A57
- Rieke G. H., et al., 2004, *ApJS*, **154**, 25
- Schütz O., Nielbock M., Wolf S., Henning T., Els S., 2004, *A&A*, **414**, L9
- Scott K. S., et al., 2008, *VizieR Online Data Catalog*, **738**
- Scott K. S., et al., 2012, *MNRAS*, **423**, 575
- Shimizu I., Yoshida N., Okamoto T., 2012, *MNRAS*, **427**, 2866
- Smail I., Ivison R. J., Blain A. W., 1997, *ApJ*, **490**, L5
- Thureau N. D., et al., 2014, *MNRAS*, **445**, 2558
- Williams J. P., Andrews S. M., 2006, *ApJ*, **653**, 1480
- Wilson G. W., et al., 2008, *MNRAS*, **386**, 807
- Wyatt M. C., 2008, *ARA&A*, **46**, 339
- Wyatt M. C., Dermott S. F., Telesco C. M., Fisher R. S., Grogan K., Holmes E. K., Piña R. K., 1999, *ApJ*, **527**, 918
- Wyatt M. C., et al., 2012, *MNRAS*, **424**, 1206
- Zechmeister M., et al., 2013, *A&A*, **552**, A78